Stoichiometric methane conversion to ethane using photochemical looping at ambient temperature

Xiang Yu [a], Vladimir L. Zholobenko [b], Simona Moldovan [c], Di Hu [a], Dan Wu [a], Vitaly V. Ordomsky [a] and Andrei Y. Khodakov [a*]*

[a]*Univ. Lille, CNRS, Centrale Lille, Univ. Artois, UMR 8181 - UCCS - Unité de Catalyse et Chimie du Solide, F-59000 Lille, France*

[b]*School of Physical and Chemical Sciences, Keele University, Staffordshire, ST5 5BG, United Kingdom*

[c]*Groupe de Physique des Matériaux, CNRS, Université Normandie & INSA Rouen Avenue de l'Université - BP12, 76801 St Etienne du Rouvray, France*

Corresponding authors: vitaly.ordomsky@univ-lille.fr, andrei.khodakov@univ-lille.fr

Abstract

Methane activation and utilization are among the major challenges of modern science. Methane is potentially an important feedstock for manufacturing value-added fuels and chemicals. However, most of known processes require excessive operating temperatures and exhibit insufficient selectivity. Here, we demonstrate a photochemical looping strategy for highly selective stoichiometric conversion of methane to ethane at ambient temperature over silver-heteropolyacid-titania nanocomposites. The process involves stoichiometric reaction of methane with highly-dispersed cationic silver under illumination, which results in the formation of methyl radicals. Recombination of the generated methyl radicals leads to selective, and almost quantitative, formation of ethane. Cationic silver species are simultaneously reduced to metallic silver. The silver-heteropolyacid-titania nanocomposites can be reversibly regenerated in air under illumination at ambient temperature. The photochemical looping process achieves methane coupling selectivity over 90%, quantitative yield of ethane over 9%, high quantum efficiency (3.5% at 362 nm) and excellent stability.

Methane is the main component of natural and shale gas, methane clathrates and biogas, and is a potent greenhouse gas. _ENREF_1About 90% of methane is currently burnt in various combustion processes, releasing carbon dioxide into the atmosphere [1-7]. Finding ways to efficiently convert methane into fuels and chemicals is important for the rational utilization of fossil and renewable energy feedstocks, as well as for reducing the emission of greenhouse gases. Methane is a highly stable molecule; it has no functional groups and a very high C-H bond enthalpy (439 kJ mol^{-1}). Methane is also inert relative to the acid attack and it has very low proton affinity (544 kJ mol^{-1}) and acidity (pK_a=40). Therefore, direct chemical conversion of methane to value-added chemicals and fuels remains a formidable challenge for modern science [8-10].

Commercial technologies of methane utilization, other than combustion, are rather limited. They involve methane steam reforming, partial oxidation, autothermal reforming or Andrussow reaction [11-13]. The non-commercial routes for methane conversion can be divided into oxidative and non-oxidative ones [8-21]. The non-oxidative routes, such as methane aromatization, result in significant carbon deposition, while the oxidative routes, such as methane thermocatalytic coupling and methane partial oxidation, usually suffer from insufficient selectivity and abundant production of CO_2. Most of the known methane conversion reactions require very high temperatures (>800°C). Generally, these thermochemical processes are accompanied by CO_2 emissions arising from the combustion of fossil fuels utilized to maintain the reactor at high temperatures[18-23].

Photocatalytic non-oxidative coupling of methane with very low quantum efficiencies and yields was observed over silica, highly dispersed Ga or Ce species [24-26]. Activation of methane over Zn^{2+}/ZSM-5 and Ga^{3+}/EST-10 photocatalysts has been reported, with the photocatalytic

activity attributed to the presence of extra-framework zinc cations and Ti-OH groups on titanate wires [27,28]. Photocatalytic non-oxidative coupling of methane has been observed when exploiting the surface plasmon effect of Au [29] or Ga and Pt photocatalysts supported on TiO_2-SiO_2 [30]. Methane photocatalytic coupling with higher quantum efficiencies has been reported over Pd/TiO_2 catalysts [31,32]. A photoelectrochemical system has also been used [33], however, the maximum selectivity of methane coupling to ethane was below 53%. Thus, the major challenges of methane coupling in both thermocatalytic and photocatalytic routes are insufficient selectivities and yields of target products, large production of CO_2 and poor catalyst stability.

In this work, we demonstrate a photochemical looping concept for methane conversion to ethane at ambient temperature under irradiation using silver-heteropolyacid-titania nanocomposites, which achieves high selectivity (>90%), significant yield of C_2H_6 (>9%), high quantum efficiency (QE = 3.5% at 362 nm) and excellent stability.

Photochemical coupling of methane over metal nanocomposites

First, we investigated photochemical conversion of methane over TiO_2, HPW and HPW/TiO_2 composites containing different metals in a batch photoreactor (**Supplementary Fig. 1**). HPW refers to phosphotungstic acid. No methane conversion was observed in the absence of light on all the studied solids. In agreement with previously reported data [34], CO_2 was detected as the only reaction product after exposure of TiO_2, HPW and HPW/TiO_2 composites to methane at ambient temperature using the illumination (**Fig. 1**). As the gaseous phase in the reactor contained only methane, but no oxygen or other gases, the oxygen for the methane oxidation to CO_2 must have been provided by the solids (TiO_2, HPW, etc) present in the photoreactor.

Methane conversion over the metal containing HPW/TiO_2 composites yields both C_2H_6 and CO_2 (**Fig. 1a**), along with traces of CO, while no hydrogen or oxygen were detected. Lower methane coupling production was observed over the solids containing Cu, Zn and Bi. Higher production rate and selectivity to ethane were observed on the Pt, Au and Ag based HPW/TiO_2 nanocomposites. Besides ethane, small amounts of propane were detected. Remarkably, compared to the Pt- and Au-based counterparts, Ag-HPW/TiO_2 demonstrated much higher ethane selectivity and methane conversion rate. The overall selectivity of methane coupling to ethane and propane is greater than 90% on the Ag-HPW/TiO_2 nanocomposite. Note that the silver salt of heteropolyacid deposited on TiO_2 (AgPW/TiO_2*)* exhibits similar performance in methane coupling (**Fig. 1b**). After exposure to methane in the presence of light, the Ag-HPW/TiO_2 sample becomes black, indicating possible photochemical transformation of oxidized silver species to silver metallic phase (**Fig. 2a,b**).

Apart from GC analysis, the composition of the gaseous phase during the methane conversion was followed by *in-situ* FTIR (**Supplementary Fig. 2)**. Only methane was detected at the initial period of reaction. Gaseous CO_2 and H_2O were identified in the FTIR cell at later stages with the intensity of the H_2O and CO_2 bands noticeably increasing with the reaction time.

In order to confirm the importance of irradiation for methane coupling, we exposed the Ag-HPW/TiO_2 nanocomposite in the absence of irradiation to methane at 100°C. No methane conversion was observed in the absence of light. To evaluate the effect of chemisorbed water and oxygen on methane conversion, the Ag-HPW/TiO_2 composite was heated overnight at 80°C. No effect of this dehydration pretreatment on the reaction selectivity was observed.

We attempted to optimize the chemical composition of silver containing nanocomposites by varying the silver content, HPW/TiO_2 ratio, supports (TiO_2, SiO_2, g-C_3N_4 and $BiVO_4$) and

heteropolyacid (phosphotungstic, phosphomolybdic and silicotungstic). The addition of even 1 wt. % of silver to HPW/TiO_2 results in a major increase in the rate of methane coupling. The highest rate was observed at the Ag content of 6.0 wt. %, the rate then decreased at higher Ag loadings (**Supplementary Fig. 3**). In the sample with 6 wt. % Ag content, the optimized performance was obtained at the HPW/TiO_2 ratio of 0.6, while the methane coupling rate decreases at higher HPW/TiO_2 ratios (**Supplementary Fig. 4**). One of the reasons for lower methane coupling rate could be the decline of the specific surface area measured by BET at the higher content of heteropolyacid (**Supplementary Table 1**). We observed ethane production, but with low efficiency over silver species dispersed in silica and other insulator supports (**Supplementary Fig. 5**). This is also consistent with previous research [35, 36], reporting small amounts of ethane forming from methane over silver-containing zeolites. The amounts of ethane, propane and carbon dioxide produced over the silver-titania nanocomposite containing different heteropolyacids as a function of reaction time are shown in **Supplementary Fig. 6.** Ethane and propane are produced with higher yield only in the presence of phosphotungstic acid (HPW).

Thus, a major increase in the C_2H_6 production from methane only occurs when the nanocomposite combines together TiO_2, HPW and Ag. HPW has been discovered previously [37-41] as highly efficient for transfer of holes and electrons from TiO_2. The photochemical performance of the HPW/TiO_2 nanocomposite can be enhanced by *p-n* semiconductor heterojunction, created by the addition of a semiconductor with lower levels of valence and conduction bands to TiO_2. One of the conditions for heterojunction is close contact but distinct separation of two semiconductor phases. The valence and conduction bands of phosphotungstic acid are located at a lower energy than that for TiO_2, which may result in a higher electron flux

from TiO_2 onto HPW (**Supplementary Figure 7**). In the presence of irradiation and electric field, the electrons are transferred to the conduction band of the p-type semiconductor (HPW) and the holes to the valence band of the n-type semiconductor (TiO_2). This heterojunction increases the electron concentration in HPW and hole concentration in TiO_2. Methane oxidation is then improved by the higher concentration of holes on the surface of TiO_2, while silver reduction is enhanced by higher electron density over HPW. Note that ethane also forms over Ag-HPW though with lower rate compared to the Ag-HPW-TiO_2 nanocomposite. This emphasizes an additional important role of HPW in dispersing silver species.

Characterization of the Ag-HPW/TiO_2 nanocomposites

X-ray diffraction (XRD) patterns of Ag-HPW/TiO_2, Ag/TiO_2, HPW/TiO_2, TiO_2 and HPW are shown in **Fig. 3a**. All the samples supported over TiO_2 exhibit intense XRD peaks of anatase and rutile phases, while the peaks assigned to the heteropolyacid are only observed in the XRD patterns of the pure HPW sample. Interestingly, neither HPW, nor silver diffraction peaks were detected in the Ag-HPW/TiO_2 nanocomposite even at a relatively high silver content, which is probably due to higher dispersion of both HPW and silver species.

The TEM, STEM-HAADF and STEM-EDX elemental maps of the Ag-HPW/TiO_2 sample are shown in **Fig. 4** and **Supplementary Fig. 8.** They identify irregular morphology of TiO_2 crystallites with the mean sizes of 30-40 nm. The STEM-EDX tungsten maps indicate the formation of a thin layer of HPW (1-2 nm) embedded over the TiO_2 crystals. Extremely small silver nanoparticles (probably present as silver oxide species) with the mean diameter of 1.9 nm are uniformly dispersed on the surface of HPW/TiO_2 (**Fig. 4b**). Note that the Ag-HPW/TiO_2 sample could also contain silver cations in the cationic sites of the heteropolyacid, which cannot

be conclusively detected by TEM for this particular system.

The TPR profiles of HPW/TiO_2-based nanocomposites are shown in **Supplementary Fig. 9**. The introduction of silver results in the occurrence of additional low temperature TPR peaks at 400 K for both Ag/TiO_2 and Ag-HPW/TiO_2 samples, which are attributed to the reduction of silver species:

$2Ag^+ + H_2 \rightarrow 2Ag^0 + 2H^+$

The UV-Vis diffuse reflectance spectra of Ag-HPW/TiO_2, Ag-HPW/SiO_2 and reference compounds (**Supplementary Fig. 10**) exhibit intense absorption in the ultraviolet region. The band gap energy, estimated using Tauc's plots, varies from 2.8 eV to 3.2 eV [42-44]. Note that the value of band gap in TiO_2 is close to that in HPW [34, 41]. Interestingly, a much smaller band gap was observed in Ag-HPW/SiO_2 compared to Ag-HPW/TiO_2. This can be assigned to lower dispersion and larger domain sizes of HPW on the SiO_2 support. Indeed, the bandgap in supported oxide clusters and heteropolyacids decreases with the increase in the particle size[45, 46].

Table 1. Rate of photochemical methane coupling measured under irradiation at different spectral ranges.

Spectral range of irradiation (nm)	**Formation rate (μmol g^{-1} h^{-1})**		**Irradiance（mW cm^{-2}）**	**Formation rate to power ratio (μmol g^{-1} h^{-1} mW^{-1} cm^2)**
	C_2H_6	C_3H_8		
>382	0.7	0.0	94	0.0074
280-400	23	1.2	38	0.64

Reaction conditions: solid sample, 0.1 g; Gas phase pressure, CH_4 0.3 Mpa; irradiation time, 7h; light source, Hamamatsu LC8-06 Hg-Xe stabilized irradiation lamps with a spectral irradiance in the range 240-600; Cut-off filter: Vis-IR λ > 382 nm; UV light, λ = 280-400 nm.

To evaluate the influence of UV, visible and IR light on methane coupling, we conducted photochemical experiments using selected spectral ranges (280<λ<400 nm and λ>400 nm,

Table 1). The Ag-HPW/TiO_2 nanocomposite exhibits a lower reaction rate under visible-IR irradiation, while the reaction rate increases 90 times upon the exposure to the UV light. The excitation of the band gap transfer in TiO_2 seems necessary for this photochemical process.

Reaction pathways in photochemical coupling of methane

To explore the molecular pathways of photochemical methane coupling, Ag-HPW/TiO_2 was exposed to methane, ethane or a mixture of methane and ethane under irradiation (**Fig. 5).** Ethane and propane were observed during the photochemical conversion of methane, along with small amounts of CO_2. The exposure of Ag-HPW/TiO_2 to ethane under irradiation led to some amounts of butane, whilst CO_2 became the main product. When the reactor contained a mixture of 5% ethane and 95% methane, ethane with propane and butane were produced under the Xe-lamp irradiation. This is indicative of simultaneous ethane self-coupling and ethane-methane cross-coupling over Ag-HPW/TiO_2, though the selectivity to higher hydrocarbons in the ethane coupling is much lower, because of the competing complete oxidation of ethane and higher hydrocarbons. The Ag-HPW/TiO_2 nanocomposite was also exposed to propane under irradiation. No propane coupling was detected, only CO_2 was observed as the reaction product. Notably, the addition of hydroquinone, a well-known inhibitor of radical reactions [47], resulted in a major decrease in the methane conversion over Ag-HPW/TiO_2, implying that methane oxidative coupling proceeds via radical pathways involving CH_3 radicals as intermediates.

The variation of the amount of ethane, propane and CO_2 with time during exposure of Ag-HPW/TiO_2 to light in the presence of methane (**Supplementary Fig. 11a**) shows a sharp increase in the concentration of ethane during the first 2 h of the reaction. In the experiments conducted with different amounts of Ag-HPW/TiO_2, the molar amount of produced ethane was

always comparable with that of silver present in the reactor. Extrapolation to zero reaction time gives the overall selectivity to ethane and propane greater than 90% (**Supplementary Fig. 11b**) The ethane and propane selectivities decrease and CO_2 selectivity increases with the reaction time. This suggests CO_2 production by secondary oxidation of ethane, and propane. Indeed, complete oxidation of ethane under the same conditions proceeds easier than that of methane (**Fig. 5**).

To provide further insights into the variation of silver oxidation state during the reaction, both the freshly calcined Ag-HPW/TiO_2 nanocomposite and its spent counterpart have been characterized by XRD, XPS and FTIR. Note that the amount of ethane produced in the second reaction cycle, without sample regeneration, was much lower than in the first cycle (**Fig. 2c**), most probably because of the lower concentration of silver cations and presence of metallic silver, which is inactive in methane coupling. The nanocomposite exposure to methane under irradiation results in the XRD peaks at 2θ of 44.48°, 64.69° and 77.62°(**Fig. 3b**), which correspond to the 200, 220, and 311 planes of metallic silver [48]. When the solid material is regenerated in air under the Xe-lamp irradiation for 2 h, the XRD peaks of metallic silver almost disappear. XPS and Auger spectroscopy provided further insights into the silver oxidation state in the fresh and spent materials[49-53]. In the Ag Auger spectrum of Ag-HPW/TiO_2 (**Fig. 2d**) recorded after treatment in 0.3 MPa CH_4 under Xe-lamp irradiation for 7 h, the $M_4N_{45}N_{45}$ (M_4VV) peak shifts to lower binding energy by 1.9 eV. For the regenerated sample, the peak returns to its initial position. These results are indicative of reversible reduction and re-oxidation of highly dispersed silver species, which take place under irradiation, respectively in methane or air.

The variation of Brønsted and Lewis acidity during methane coupling was monitored using

FTIR experiments with adsorbed pyridine (**Fig. 2e**). The IR spectrum of the fresh oxidized HPW/TiO_2 shows the bands of adsorbed Py at 1540 and 1444 cm^{-1} attributed to Py adsorption over the Brønsted and Lewis acid sites[54] (BAS and LAS, respectively). The HPW/TiO_2 sample contains 166 μmol/g of BAS and 36 μmol/g of LAS. The silver salt of HPW deposed over TiO_2 is expected to have the highest concentration of silver in the cationic sites of HPW. As expected, the introduction of silver cations results in a decrease in the number of BAS to 10 μmol/g and increase in the number of LAS to 154 μmol/g in the freshly calcined catalysts. The Py band attributed to LAS shifts to 1447 cm^{-1} indicating the formation of LAS associated with low-coordinated Ag^+ ions. The exposure of AgPW/TiO_2 to methane under irradiation results in the reappearance of the Py bands attributed to BAS following the reduction of silver species:

$$2Ag^+ + 2CH_4 \rightarrow C_2H_6 + Ag^0 + 2H^+$$

After the reaction, the number of BAS in AgPW/TiO_2 increased to 104 μmol/g, while the number of LAS decreased to 83 μmol/g. The FTIR experiments suggest, therefore, reversible photoreduction and reoxidation of silver ions located in the cationic sites of HPW. The participation of silver cations, located in HPW, in methane selective coupling to ethane is consistent with the very high selectivity to ethane obtained under the Xe-lamp irradiation for AgPW/TiO_2 (**Fig. 1b**). It is also in agreement with the observed decrease in the rate of methane coupling at higher silver contents. Indeed, a higher silver content would result in the lowered concentrations of silver cations and an increased fraction of silver oxide clusters (analogous to the Ag/TiO_2 sample), which are less selective in methane coupling, possibly promoting secondary oxidation. As the coupling reaction involves two CH_3 radical species produced via methane activation over silver sites, the proximity between two Ag^+ sites is likely to affect methane conversion, thereby explaining the lower relative amount of ethane produced from

methane at low silver content in Ag-HPW/TiO_2 nanocomposites (**Supplementary Fig. 3**).

Synthesis of ethane from methane via photochemical looping

The reaction tests and characterization suggest a stoichiometric photochemical reaction of methane with cationic silver species selectively yielding ethane and propane. The reaction slows down, when cationic silver species are reduced to metallic silver. In order to conduct continuously ethane synthesis from methane, the reduced silver species should be reversibly reoxidized, so that the spent Ag-HPW/TiO_2 could be reversibly regenerated. **Fig. 6a** shows photochemical conversion of methane on the spent Ag-HPW/TiO_2, which was regenerated via exposure to air under irradiation for 7 h. The rate of formation and amounts of ethane, propane and CO_2 are the same over the fresh and regenerated Ag-HPW/TiO_2 nanocomposites following 10 reaction-regeneration cycles.

A different response is observed (**Supplementary Fig. 12**) during the reaction-regeneration cycles for Ag/TiO_2. Methane conversion on this solid, results in CO_2 and small amounts of ethane. The lower selectivity to ethane in methane conversion over Ag/TiO_2 is consistent with the important role of cationic silver species, rather than relatively large silver oxide clusters present in Ag/TiO_2, in achieving higher ethane selectivity. In contrast to the Ag-HPW/TiO_2 nanocomposite, the amounts of the produced CO_2 and ethane decrease in successive reaction-regeneration cycles indicating irreversible modifications of the Ag/TiO_2 structure.

Particle size measurements using TEM in fresh and spent Ag-HPW/TiO_2 and Ag/TiO_2 are displayed in **Supplementary Fig. 13**. Whilst for the used Ag/TiO_2 sample, the Ag nanoparticles became noticeably larger after the reaction and a much broader particle size distribution was observed due to sintering (3.3 ± 1.3 nm), the Ag particle size in Ag-HPW/TiO_2 was essentially

unchanged following reaction and regeneration. Thus, the presence of HPW stabilizes high silver dispersion, while silver sintering is the major reason for the decrease in the photochemical activity of Ag/TiO_2 after several reaction-regeneration cycles.

The uncovered stability of the $Ag\text{-}HPW/TiO_2$ nanocomposite after numerous reaction-regeneration cycles suggests that methane coupling to ethane can be conducted using looping. Previously, the looping strategy has been successfully used for several chemical reactions[55-60]. In this work, we propose a concept of "photochemical looping" (**Fig. 6b)**. During the methane-coupling step, CH_4 is fed into the reactor containing $Ag\text{-}HPW/TiO_2$ under irradiation. The interaction of methane with silver cationic species leads to the formation of metallic silver, ethane, small amounts of propane and CO_2. This reaction also generates BAS, observed by FTIR, in the spent $Ag\text{-}HPW/TiO_2$ sample. In the regeneration step, $Ag\text{-}HPW/TiO_2$ is exposed to air under irradiation, which leads to re-oxidation of metallic silver:

$2CH_4 + 2Ag^+ \rightarrow C_2H_6 + 2Ag^0 + 2H^+$ methane coupling step

$4Ag^0 + O_2 + 4H^+ \rightarrow 4Ag^+ + 2H_2O$ silver regeneration step

In the photochemical looping process, $Ag\text{-}HPW/TiO_2$ reacts stoichiometrically with methane yielding ethane and higher hydrocarbons. The maximum amount of ethane and higher hydrocarbons produced during the photochemical conversion of methane depends on the amount of cationic silver in the reactor, which is reduced to the metallic state. Metallic silver is then reoxidized to cationic species under irradiation in the presence of air.

Separation of methane and ethane can be prohibitively expensive if the concentration of the target product in the post-reaction mixture is low. This is why we attempted to increase the yield of ethane in the photochemical looping by increasing the ratio of photoactive $Ag\text{-}HPW/TiO_2$ nanocomposite to methane up to 0.33 (3 μmol of silver and 9 μmol of methane). Hence, methane

coupling was conducted in a capillary photoreactor with reduced volume (**Supplementary Fig. 14**). With some decrease in the selectivity to C_{2+} hydrocarbons, the yield of ethane reached 9% (on carbon basis) after 5 h of exposure to irradiation (**Supplementary Figs. 15 and 16**).

Conclusion

Using a silver-hetetopolyacid-titania nanocomposite under illumination at room temperature, we observed coupling of methane to ethane with high yield and selectivity (90 %). We find that ethane synthesis involves stoichiometric methane reaction with highly dispersed silver cationic species. The photosensitive cationic silver species are reduced to metallic silver during the reaction. Silver cations dispersed in the HPW layer covering TiO_2 are essential for the methane coupling to ethane during the reaction. The nanocomposites can be reversibly regenerated by exposure to air at ambient temperature under irradiation. A photochemical looping strategy is proposed as a viable approach for selective quasi-quantitative synthesis of ethane and higher hydrocarbons from methane under irradiation at ambient temperature.

Methods

Chemicals

Titanium (IV) oxide (P25, TiO_2, 99.5%), amorphous silica (CARIACT Q-10, Fuji Silysia), urea (NH_2CONH_2, ≥98.0%), bismuth(III) nitrate pentahydrate ($Bi(NO_3)_3 \cdot 5H_2O$, ≥98.0%), ammonium metavanadate(V) (NH_4VO_3, 99%), sodium hydroxide (NaOH, ≥98%), nitric acid (HNO_3, 68.0-70.0%), phosphotungstic acid hydrate ($H_3O_{40}PW_{12} \cdot xH_2O$, M_w = 2880.05), phosphomolybdic acid hydrate ($H_3[P(Mo_3O_{10})_4] \cdot xH_2O$, M_w = 1825.25), tungstosilicic acid hydrate ($H_4[Si(W_3O_{10})_4] \cdot xH_2O$, M_w = 2878.17), zinc nitrate hexahydrate ($Zn(NO_3)_2 \cdot 6H_2O$, ≥

99.0%), gallium(III) nitrate hydrate ($Ga(NO_3)_3 \cdot xH_2O$, 99.9%), copper(II) nitrate trihydrate ($Cu(NO_3)_2 \cdot 3H_2O$, 99-104%), bismuth(III) nitrate pentahydrate ($Bi(NO_3)_3 \cdot 5H_2O$, ≥98.0%), silver nitrate ($AgNO_3$, ≥99.0%), palladium(II) nitrate hydrate ($Pd(NO_3)_2 \cdot xH_2O$, 99.9%), ruthenium(III) chloride hydrate ($RuCl_3 \cdot xH_2O$, 38.0-42.0% Ru basis), hydrogen hexachloroplatinate(IV) solution (H_2PtCl_6, 8 wt. % in H_2O) and gold(III) chloride hydrate ($HAuCl_4 \cdot aq$, ~50% Au basis) were purchased from Sigma-Aldrich and used without further purification.

Supports

Commercial amorphous silica (CARIACT Q-10, Fuji Silysia) and TiO_2 (P25) together with the synthetized g-C_3N_4 and $BiVO_4$ were used as supports for the preparation of metal-heteropolyacid nanocomposites. g-C_3N_4 was fabricated by calcining urea. The powder of urea was calcined in a muffle furnace for 2 h at 550 °C with a ramping rate of 10 °C min^{-1} in air. After cooling down to room temperature, the final light-yellow g-C_3N_4 was obtained. Monoclinic $BiVO_4$ crystals were synthesized by a hydrothermal method. Briefly, the precursors NH_4VO_3 (0.015 mol) and $Bi(NO_3)_3 \cdot 5H_2O$ (0.015 mol) were dissolved in an aqueous nitric acid solution (2 M), and the pH value of the solution was adjusted to 2.0 with ammonia solution (14.8 M) under continuous stirring. An orange precipitate appears over time. After that, the suspension was transferred to a Teflon-lined stainless-steel autoclave with a capacity of 100 mL and treated by hydrothermal at 473 K for 24 h. After the autoclave was cooled down to room temperature, the yellow powdery sample was separated by filtration, washed with deionized water for several times, and then dried at 353 K in air for overnight. Finally, the sample was calcined at 773 K in air for 2 h. The final yellow $BiVO_4$ was obtained.

Synthesis of the metal-HPW/TiO_2 nanocomposites

The metal-HPW/TiO_2 nanocomposites were prepared by the two-step impregnation of TiO_2. During the impregnation, a fixed amount of TiO_2 was first suspended in an anhydrous ethanol solution of phosphotungstic acid hydrate ($H_3[P(W_3O_{10})_4]$ xH_2O, HPW), tungstosilicic acid hydrate ($H_4[Si(W_3O_{10})_4] \cdot xH_2O$, HSiW) and phosphomolybdic acid hydrate ($H_3[P(Mo_3O_{10})_4] \cdot xH_2O$, HPMo). The HPW to TiO_2 ratio varied from 0.15 to 1.2. The HPW/TiO_2 (HPW/TiO_2 ratio=0.6) sample was obtained by stirring. The resulting material was then dried at 353 K for 12 h. Next, the Ag-HPW/TiO_2 sample was prepared by incipient wetness impregnation of the HPW/TiO_2 support with aqueous solutions of silver nitrate ($AgNO_3$). Other metal-HPW/TiO_2 composites were prepared using impregnation with the aqueous solutions of relevant salts. The target metal content in the final materials was 6 wt. %. After the second impregnation, the samples were dried overnight at 373 K. Then, they were calcined in air at 300 °C for 3 h with the 2 °C/min temperature ramp. The samples were labelled as M-HPW/TiO_2, where M stands for Zn, Cu, Ga, Bi, Ru, Pd, Pt, Au or Ag.

Preparation of the reference silver salt of HPW deposited on TiO_2 (AgPW/TiO_2)

First, a fixed amount of phosphotungstic acid hydrate ($H_3[P(W_3O_{10})_4]$ xH_2O, HPW) was dissolved in ethanol and mixed with silver nitrate ($AgNO_3$) aqueous solution. The precipitate silver salt has been filtered out and mixed with necessary amount of TiO_2 to provide the same amount of Ag as in Ag-HPW/TiO_2 catalyst. The obtained catalyst was dried overnight at 353K and calcined at 473K in an oven.

Characterization

A combination of techniques was used for extensive characterization of the solids. The X-ray powder diffraction (XRD) patterns were measured in the 5−80° (2 θ) range using Cu K_α radiation (λ = 0.1538 nm) on a Bruker AXS D8 instrument. A Perkin-Elmer Lambda 650 S UV/VIS spectrometer with an integrating sphere covered with $BaSO_4$ as a reference was used for diffuse reflectance UV-visible spectra measurements. The BET surface area was determined by low temperature N_2 adsorption using a Micromeritics TriStar II PLUS automated system. The Transmission Electron Microscopy (TEM) observations were performed on a Tecnai instrument equipped with a LaB6 crystal and a double corrected Cold FEG ARM Jeol 200 field emission gun, operating at 200 kV. Prior to the analysis, the samples were dispersed by ultrasounds in ethanol for 5 min, and a drop of the suspension was deposited onto a carbon membrane on a 300 mesh-copper grid. The microscopy based chemical analyses were carried out in the scanning TEM mode using a 100-mm Centurio detector for the energy dispersive X-rays (EDX). The point-to-point resolution was 0.9 Å under the STEM mode. The EDX elemental maps were obtained using scanning time of 20 μs/px for imaging and 0.05 μs/px for EDX (256x256px maps), with a 0.1 nm probe size and a current of 120pA. To achieve a high signal to noise ratio the chemical maps were acquired for at least 60 minutes, along which a cross-correlation algorithm was applied every 30 seconds to correct the specimen spatial drift. The H_2 temperature-programmed reduction (H_2-TPR) was carried out using the AutoChem II 2920 apparatus (Micromeritics) in a flow of H_2/Ar (5 vol% H_2, 30 cm^3/min) with the temperature rate of 10 °C/min.

FTIR spectra were collected using a Thermo Nicolet 8700 spectrometer equipped with a MCT detector using a range of resolution setting (1 to 4 cm^{-1}). The analyzed samples were pressed in

~20-30 mg (D=13 mm) self-supporting discs and treated in vacuum at 80 °C. Pyridine (Py) adsorption has been performed by adding 5 Torr of Py with subsequent treatment under vacuum. The spectra were analyzed using specialized Thermo software (Omnic). The numbers of BAS and LAS were calculated from the Py adsorption data. The molar extinction coefficients of 1.65 cm μmol^{-1} for BAS-Py complexes and 1.87 cm μmol^{-1} for LAS-Py complexes were used for the quantification of Brønsted and Lewis acid sites.

Kratos Axis spectrometer, equipped with an aluminum monochromator for a 1486.6 eV source working at 120 W was used in this work for the XPS acquisition. The value of the Ag $3d_{5/2}$ binding energy does not allow a clear discrimination of the silver oxidation state. The Ag $3d_{5/2}$ lines of metallic Ag and silver oxide are positioned at 368.2 eV and 367.8 eV, respectively[50]. Such a small difference in the binding energy is often beyond the resolution of the XPS spectrometer, therefore Auger spectroscopy measurements were carried out. The energy of Auger peaks $M_4N_{45}N_{45}$ (M_4VV) is known to be particularly sensitive to the oxidation state differing by more than 1 eV for Ag^+ vs. Ag^0 [51-53]. The binding energies were corrected with respect to C 1s (284.6 eV), they were estimated within ± 0.2 eV. The positions of all Auger peaks were aligned by the C 1s peak, and a Shirley background was subtracted.

Photochemical tests

A homemade stainless-steel batch reactor (volume≈250 mL) with a quartz window on the top of the reactor was used for the photochemical methane conversion (**Supplementary Fig. 1**). All the photochemical tests were performed at ambient temperature. The light source for most experiments was a 400 W Xe lamp (Newport) characterized by a broad emission spectrum (from ~200 to 1100 nm). A Hamamatsu spot light source LC8-06 Hg-Xe lamp, emitting

between 240 and 600 nm, equipped with a quartz light-guide to deliver a stable and uniform illumination of the sample were used for measuring the Quantum Efficiency (QE). A Hamamatsu optical filter was used for selecting the spectral range. The irradiance measured by an optical power meter (Newport PMKIT) were 94 and 38 mW cm^{-2} in the ranges of >382 nm and 280-400 nm, respectively.

0.1 g of a solid nanocomposite was placed on a quartz glass holder at the bottom of the reactor. Then, the reactor was evacuated using a vacuum pump and filled with CH_4. The methane pressure was increased up to 0.3 MPa and the reactor was kept in the dark for 1 h to ensure an adsorption-desorption equilibrium between the solid material and reactants. Subsequently, the reactor was irradiated by the 400 W Xe lamp. The reaction time was varied between 2 and 20 h.

A photoreactor with reduced volume was used in order to obtain high methane conversion (**Supplementary Fig. 14**). This photoreactor is a quartz capillary with the internal diameter of 0.8 mm, 50 mm in length, attached to a metallic frame with epoxy glue and filled with methane (P=0.2 MPa). The weight of the Ag-HPW/TiO_2 nanocomposite in the photoreactor was 5 mg. The reaction products (C_2H_6, C_3H_8 and CO_2) were analyzed by gas chromatography (PerkinElmer Clarus 580 GC) with helium as carrier gas. The standard deviation in GC analysis was close to 5%. The reactors were attached to an on-line GC injection valve, and the gaseous products were directly injected into the GC. PoraBOND Q and ShinCarbon ST 100/120 columns, a flame ionization detector (FID) and a thermal conductivity detector (TCD) were employed for the analysis.

Measurement of quantum efficiency

The quantum efficiency (QE) at 362 nm in methane coupling was measured for the 6 wt. % Ag-HPW/TiO_2 nanocomposite. The following equation was used for the quantum efficiency (η) calculation:

$$\eta = \frac{R(\text{electron}) * N_A}{E_\lambda(J/\text{mol}) * I(W) * S(m^2) / t(s)} * 100\%$$

where N_A, I, S and t stand for the Avogadro's constant, light irradiance on the sample, irradiation area and reaction time, respectively. E_λ is given by hc/λ (λ = 362 nm). R(electron) represents the number of electrons used in the formation of the products. R_{C2}(electron) and R_{C3}(electron) are the number of moles of electrons used for the formations of C_2H_6 and C_3H_8, respectively. $R(\text{electron}) = R_{C2}(\text{electron}) + R_{C3}(\text{electron}) = 2n(C_2H_6) + 3n(C_3H_8)$, where $n(C_2H_6)$ and $n(C_3H_8)$ are the number of moles of C_2H_6 and C_3H_8, respectively.

Acknowledgments

The authors thank Laurence Burylo, Pardis Simon and Martine Frère for help with XRD and XPS measurements. X.Y. and D.H thank the Chinese scholarship council for providing stipends for their PhD studies in France. Chevreul Institute (FR 2638), Ministère de l'Enseignement Supérieur, de la Recherche et de l'Innovation, Hauts-de-France Region and FEDER are acknowledged for supporting and funding partially this work.

Author contributions

X.Y., V.V.O. and A.Y.K. conceived the idea for this work. All authors contributed to the design of the experimental setup and experimental procedures. X.Y. prepared the nanocomposite materials, collected the data and performed ex-situ characterization. X.Y, D.W., V.L.Z. and

V.V.O performed IR measurements. S.M. performed nanocomposite characterization using imaging techniques. V.L.Z., A.Y.K and X.Y. designed the capillary photoreactor and performed high conversion methane experiments. D.H. synthetized the silver salt of HPW and conducted additional experiments in order to address the reviewer comments. X.Y. and A.Y.K. wrote the draft and all the authors worked on improving the manuscript.

Additional information: Supplementary Information is available for this this paper.

Competing interests: The authors declare no competing interests.

Data availability: All essential experimental data generated or analyzed during the current study are presented in the paper and Supplementary Information files. Additional datasets related to this study are available from the corresponding authors upon reasonable request.

References

1. McFarland, E. Unconventional chemistry for unconventional natural gas. *Science* **338**, 340-342 (2012).

2. Tang, P., Zhu Q., Wu, Z. & Ma, D. Methane activation: the past and future. *Energ. Environ. Sci.* **7**, 2580-2591 (2014).

3. Taarning, E. et al. Zeolite-catalyzed biomass conversion to fuels and chemicals. *Energ. Environ. Sci.* **4**, 793-804 (2011).

4. Dapsens, P.Y., Mondelli, C. & Pérez-Ramírez, J. Biobased chemicals from conception toward industrial reality: lessons learned and to be learned. *ACS Catal.* **2**, 1487-1499 (2012).

5. Kondratenko, E.V., Mul, G., Baltrusaitis, J., Larrazábal, G.O. & Pérez-Ramírez, J. Status and perspectives of CO_2 conversion into fuels and chemicals by catalytic, photocatalytic and electrocatalytic processes. *Energ. Environ. Sci.* **6**, 3112-3135 (2013).

6. Kondratenko, E. V. et al. Methane conversion into different hydrocarbons or oxygenates: current status and future perspectives in catalyst development and reactor operation. *Catal. Sci. Technol.* **7**, 366-381 (2017).

7. Kaygusuz, K. Global energy issues, climate change and wind power for clean and sustainable energy development. *Journal of Engineering Research and Applied Science* **4**, 317-327 (2015).

8. Farrell, B.L., Igenegbai, V.O. & Linic, S. A viewpoint on direct methane conversion to ethane and ethylene using oxidative coupling on solid catalysts. *ACS Catal.* **6**, 4340-4346 (2016).

9. Hammond, C., Conrad, S. & Hermans, I. Oxidative methane upgrading. *ChemSusChem*

5, 1668-1686 (2012).

10. Choudhary, T.V. & Choudhary, V.R. Energy efficient syngas production through catalytic oxy methane reforming reactions. *Angew. Chem. Int. Ed.* **47**, 1828-1847 (2008).

11. Song, H., Meng, X.G., Wang, Z.J., Liu, H.M. & Ye, J.H. Solar-Energy-Mediated Methane Conversion. *Joule* **3**, 1606-1636 (2019).

12. Jang, W.J., Shim, J.O., Kim, H.M., Yoo, S.Y. & Roh, H.S. A review on dry reforming of methane in aspect of catalytic properties. *Catal. Today* **324**, 15-26 (2019).

13. Lunsford, J.H. Catalytic conversion of methane to more useful chemicals and fuels: a challenge for the 21st century. *Catal. Today* **63**, 165-174 (2000).

14. Webb, J.R., Bolaño, T. & Gunnoe, T.B. Catalytic Oxy Functionalization of Methane and Other Hydrocarbons: Fundamental Advancements and New Strategies. *ChemSusChem* **4**, 37-49 (2011).

15. Wang, B., Albarracín-Suazo, S., Pagán-Torres, Y. & Nikolla, E. Advances in methane conversion processes. *Catal. Today* **285**, 147-158 (2017).

16. Keller, G. & Bhasin, M. Synthesis of ethylene via oxidative coupling of methane: I. Determination of active catalysts. *J. Catal.* **73**, 9-19 (1982).

17. Zavyalova, U., Holena, M., Schlögl, R. & Baerns, M. Statistical analysis of past catalytic data on oxidative methane coupling for new insights into the composition of high performance catalysts. *ChemCatChem* **3**, 1935-1947 (2011).

18. Stansch, Z., Mleczko, L. & Baerns, M. Comprehensive kinetics of oxidative coupling of methane over the La_2O_3/CaO catalyst. *Ind. Eng. Chem. Res.* **36**, 2568-2579 (1997).

19. Lunsford, J.H. The catalytic oxidative coupling of methane. *Angew. Chem. Int. Ed.* **34**,

970-980 (1995).

20. Baerns, M. & Kondratenko, E.V. Oxidative coupling of methane. In: *Handbook of Heterogeneous Catalysis. 2nd Edition*. Wiley-VCH Verlag GmbH & Co. KGaA (2008).

21. Kuo, J., Kresge, C. & Palermo, R. Evaluation of direct methane conversion to higher hydrocarbons and oxygenates. *Catal. Today* **4**, 463-470 (1989).

22. Kanai, M. Photocatalytic upgrading of natural gas. *Science* **361**, 647-648 (2018).

23. Yuliati, L. & Yoshida, H. Photocatalytic conversion of methane. *Chem. Soc. Rev.* **37**, 1592-1602 (2008).

24. Yuliati, L., Hamajima, T., Hattori, T. & Yoshida, H. Highly dispersed Ce (III) species on silica and alumina as new photocatalysts for non-oxidative direct methane coupling. *Chem. Commun.,* **38**, 4824-4826 (2005).

25. Yuliati, L., Tsubota, M., Satsuma, A., Itoh, H. & Yoshida, H. Photoactive sites on pure silica materials for nonoxidative direct methane coupling. *J. Catal.* **238**, 214-220 (2006).

26. Yuliati, L., Hattori, T., Itoh, H. & Yoshida, H. Photocatalytic nonoxidative coupling of methane on gallium oxide and silica-supported gallium oxide. *J. Catal.* **257**, 396-402 (2008).

27. Li, L. et al. Efficient Sunlight Driven Dehydrogenative Coupling of Methane to Ethane over a Zn^{+} Modified Zeolite. *Angew. Chem. Int. Ed.* **50**, 8299-8303 (2011).

28. Li, L. et al. Synergistic Effect on the Photoactivation of the Methane C-H Bond over Ga^{3+} Modified ETS 10. *Angew. Chem. Int. Ed.* **51**, 4702-4706 (2012).

29. Meng, L.S. et al. Gold plasmon-induced photocatalytic dehydrogenative coupling of methane to ethane on polar oxide surfaces. *Energ. Environ. Sci.* **11**, 294-298 (2018).

30. Wu, S.Q. et al. Ga-Doped and Pt-Loaded Porous TiO_2–SiO_2 for Photocatalytic

Nonoxidative Coupling of Methane. *J. Am. Chem. Soc.* **141**, 6592-6600, (2019).

31. Yu, L., Shao,Y. & Li, L. Direct combination of hydrogen evolution from water and methane conversion in a photocatalytic system over Pt/TiO_2, *Appl. Catal. B: Environ.* **204**, 216–223 (2017).

32. Yu, L & Li, D. Photocatalytic methane conversion coupled with hydrogen evolution from water over Pd/TiO_2. *Catal.Sci. & Techn*. **7**, 635-640 (2017).

33. Amano, F. et al. Photoelectrochemical Homocoupling of Methane under Blue Light Irradiation. *ACS Energy Letters* **4,** 502-507 (2019).

34. Yu, X., De Waele, V., Löfberg, A., Ordomsky, V. & Khodakov, A.Y. Selective photocatalytic conversion of methane into carbon monoxide over zinc-heteropolyacidtitania nanocomposites, *Nature Commun*. **10**, Article number: 700 (2019).

35. Yoshida, H., et al. *Research on Chemical Intermediates* **29**, 897–910(2003).

36. Ozin, G.A. & Hugues, F. Selective Photoactivation of Carbon-Hydrogen Bonds in Paraffinic Hydrocarbons.Dimerization of Alkanes, J. *Phys. Chem*. **86**, 5174-5179(1982).

37. Wang, H. et al. Semiconductor heterojunction photocatalysts: design, construction, and photocatalytic performances. *Chem. Soc. Rev.* **43**, 5234-5244 (2014).

38. Sun, Z., Zhang, Y., Li, N., Xu, L. & Wang, T. Enhanced photoconductivity of a polyoxometalate–TiO_2 composite for gas sensing applications. *J. Mater. Chem. C*, **3**, 6153-6157 (2015).

39. Meng, P. et al. Positive effects of phosphotungstic acid on the in-situ solid-state polymerization and visible light photocatalytic activity of polyimide-based photocatalyst. *Appl. Catal. B*, **226**, 487- 498 (2018).

40. Tran, P. D., Wong, L. H., Barberbcd, J. & Loo, J. S. C. Recent advances in hybrid

photocatalysts for solar fuel production. *Energy Environ. Sci.*, **5**, 5902-5918 (2002).

41. Yu, X., Moldovan, S., Ordomsky, V.V. & Khodakov, A.Y. Design of core–shell titania–heteropolyacid–metal nanocomposites for photocatalytic reduction of CO_2 to CO at ambient temperature. *Nanoscale Adv.* **1**, 4321-4330 (2019).

42. Gondal, M., Hameed, A., Yamani, Z. & Arfaj, A. Photocatalytic transformation of methane into methanol under UV laser irradiation over WO_3, TiO_2 and NiO catalysts. *Chem. Phys. Lett.* **392**, 372-377 (2004).

43. Murcia-López S. et al. Controlled photocatalytic oxidation of methane to methanol through surface modification of beta zeolites. *ACS Catal.* **7**, 2878-2885 (2017).

44. Murcia-López, S., Villa, K., Andreu, T. & Morante, J.R. Partial oxidation of methane to methanol using bismuth-based photocatalysts. *ACS Catal.* **4**, 3013-3019 (2014).

45. Barton, D.G., Shtein, M., Wilson, R. D., Soled, S. L. and Iglesia, E. Structure and Electronic Properties of Solid Acids Based on Tungsten Oxide Nanostructures. *J. Phys. Chem. B* **103**, 630-640 (1999).

46. Weber, R.S. Effect of local structure on the UV-visible absorption edges of molybdenum oxide clusters and supported molybdenum oxides. *J. Catal.* **151**, 470-474(1995).

47. Nakarada, Đ. & Petković, M. Mechanistic insights on how hydroquinone disarms OH and OOH radicals. *Int. J. Quantum Chem.* **118**, e25496 (2018).

48. Kalishwaralal, K., Deepak, V., Ramkumarpandian, S., Nellaiah, H. & Sangiliyandi, G. Extracellular biosynthesis of silver nanoparticles by the culture supernatant of Bacillus licheniformis. *Mater. Lett.* **62**, 4411-4413 (2008).

49. Prieto, P. et al. XPS study of silver, nickel and bimetallic silver–nickel nanoparticles

prepared by seed-mediated growth. *Appl. Surf. Sci.* **258**, 8807-8813 (2012).

50. Gaarenstroom, S. & Winograd, N. Initial and final state effects in the ESCA spectra of cadmium and silver oxides. *J. Chem. Phys.* **67**, 3500-3506 (1977).

51. Anthony, M. & Seah, M. XPS: Energy calibration of electron spectrometers. 1-An absolute, traceable energy calibration and the provision of atomic reference line energies. *Surf. Interface Anal.* **6**, 95-106 (1984).

52. Samokhvalov, A., Nair, S., Duin, E.C. & Tatarchuk, B.J. Surface characterization of Ag/Titania adsorbents. *Appl. Surf. Sci.* **256**, 3647-3652 (2010).

53. Fernández, A. & González-Elipe, A. In situ XPS study of the photoassisted reduction of noble-metal cations on TiO_2. *Appl. Surf. Sci.* **69**, 285-289 (1993).

54. Parry, E. P. An Infrared Study of Pyridine Adsorbed on Acidic Solids. Characterization of Surface Acidity. *J. Catal.* **2**, 371-379 (1963).

55. Adanez, J., Abad, A., Garcia-Labiano, F., Gayan, P. & Luis, F. Progress in chemical-looping combustion and reforming technologies. *Prog. Energ. Combust. Sci.* **38**, 215-282 (2012).

56. Bhavsar, S., Najera, M., Solunke, R. & Veser, G. Chemical looping: To combustion and beyond. *Catal. Today* **228**, 96-105 (2014).

57. Vorrias, I. et al. Calcium looping for CO_2 capture from a lignite fired power plant. *Fuel* **113**, 826-836 (2013).

58. Galvita, V.V, Poelman, H. & Marin, G.B. Combined chemical looping for energy storage and conversion. *J. Power Sources* **286**, 362-370 (2015).

59. Buelens, L.C., Galvita, V.V., Poelman, H., Detavernier, C. & Marin, G.B. Super-dry reforming of methane intensifies CO_2 utilization via Le Chatelier's principle. *Science*

354, 449-452 (2016).

60. Zhang, J., Haribal, V. & Li, F. Perovskite nanocomposites as effective CO_2-splitting agents in a cyclic redox scheme. *Sci. Adv.* **3**, e1701184 (2017).

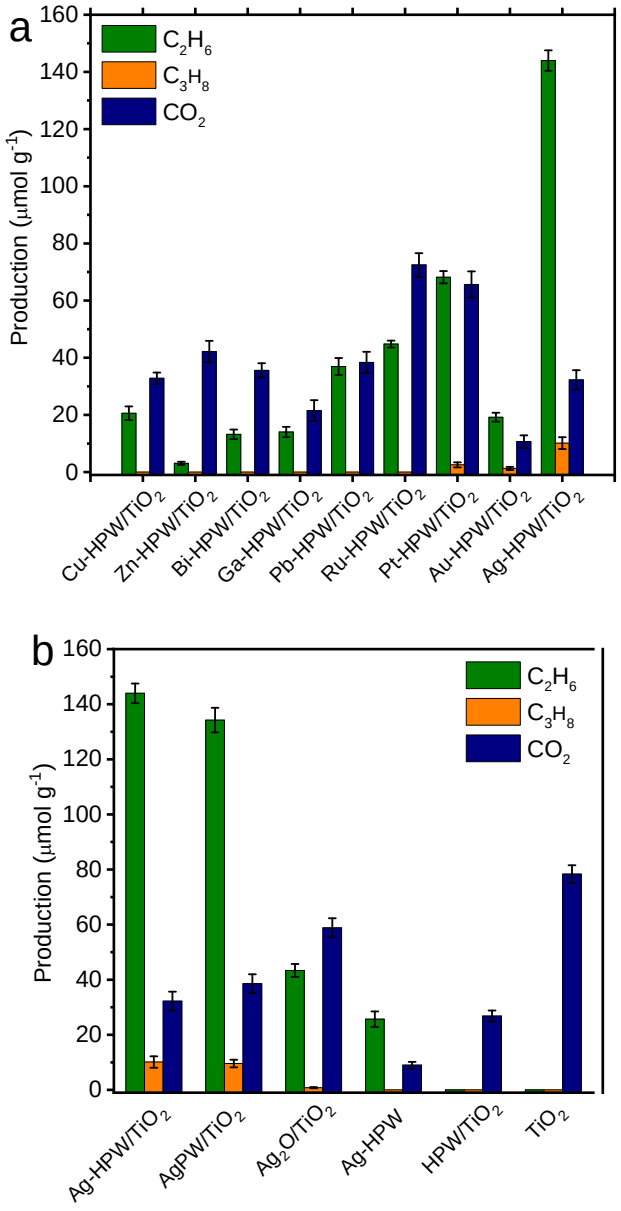

Figure 1. Photochemical coupling of methane on different materials (a) Metal-HPW/TiO_2 composite, (b) TiO_2, HPW, and Ag containing samples. Reaction conditions: catalyst, 0.1 g; gas phase pressure, CH_4 0.3 MPa; irradiation time, 7 h. The selectivity was calculated on a molar carbon basis. The experiments in each case were performed for three times. The error bar represents the relative standard deviation, which is within 5%.

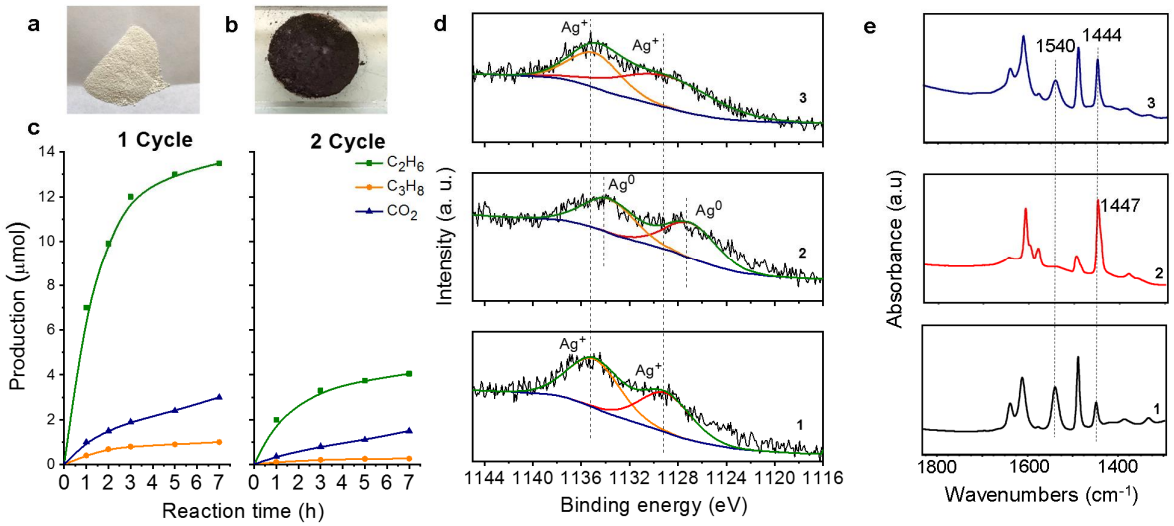

Figure 2. Changes of Ag-HPW/TiO_2 after methane photochemical coupling (a) Photo of the fresh catalyst. (b) Photo of the spent catalyst. (c) Methane photochemical coupling on fresh and spent Ag-HPW/TiO_2. The lines are guides to the eye. Reaction conditions: catalyst, 0.1 g; gas phase pressure, CH_4 0.3 MPa. (d) Ag M_4VV Auger spectra of Ag-HPW-TiO_2: fresh sample (1), sample treated in 0.3 MPa CH_4 under 400 W Xe lamp for 7h (2), sample regenerated in ambient air under 400 W Xe lamp for 2h (3). d) FTIR of Py adsorbed over HPW/TiO_2 (1), fresh (2) and spent AgPW/TiO_2 (3) showing generation of HPW Brønsted acidity during the methane coupling

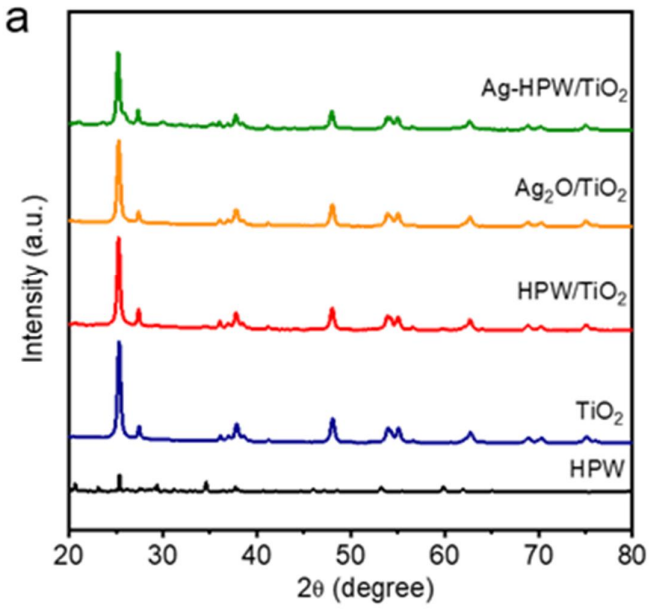

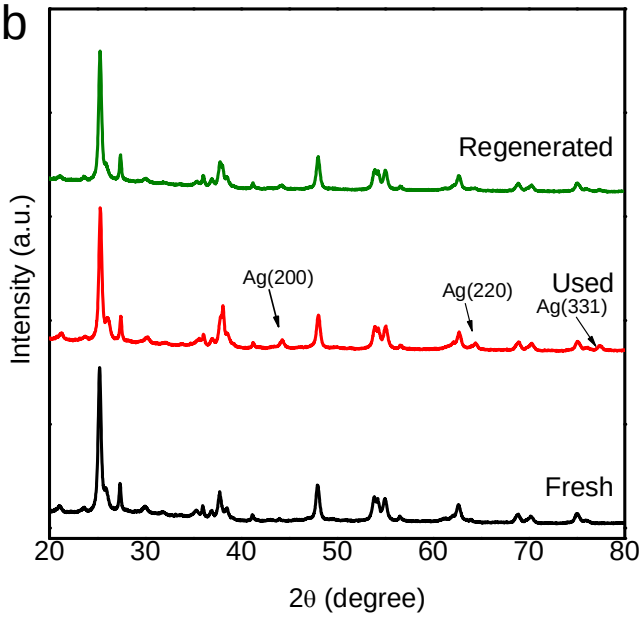

Figure 3. XRD patterns (a) different calcined nanocomposites. (b) fresh, treatment in 0.3 Mpa CH_4 under 400 W Xe lamp for 7h, and regenerate catalyst: regeneration in ambient air under 400 W Xe lamp for 2 h.

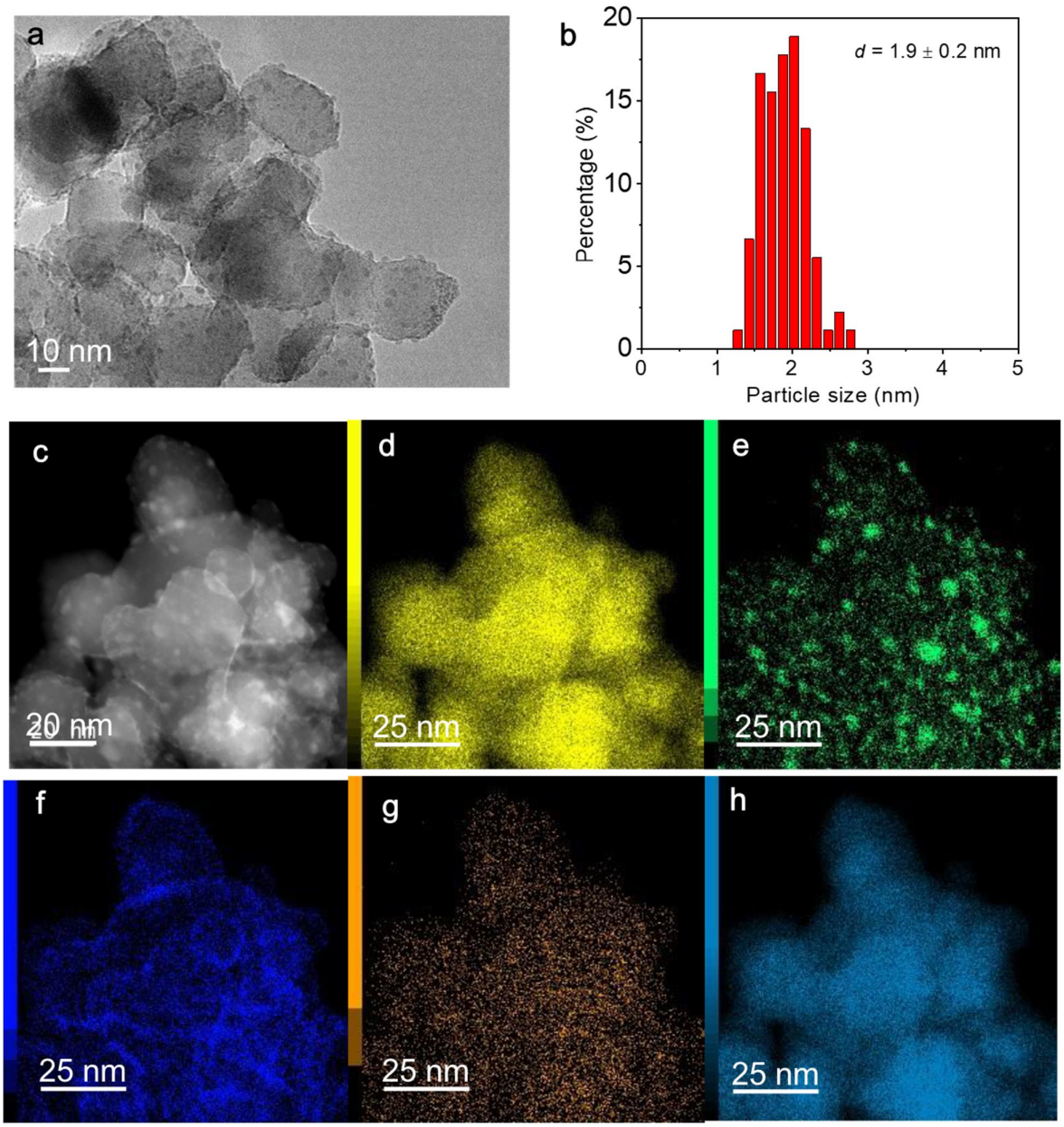

Figure 4. TEM and EDX mapping images of fresh Ag-HPW/TiO_2 sample (a) TEM image. (b) Ag particle size distribution. (c) STEM and corresponding EDX mapping images with intensity scale corresponding to the concentration of the elements and edge: Ti K (d), Ag L (e), W M (f), P K (g), O K (h).

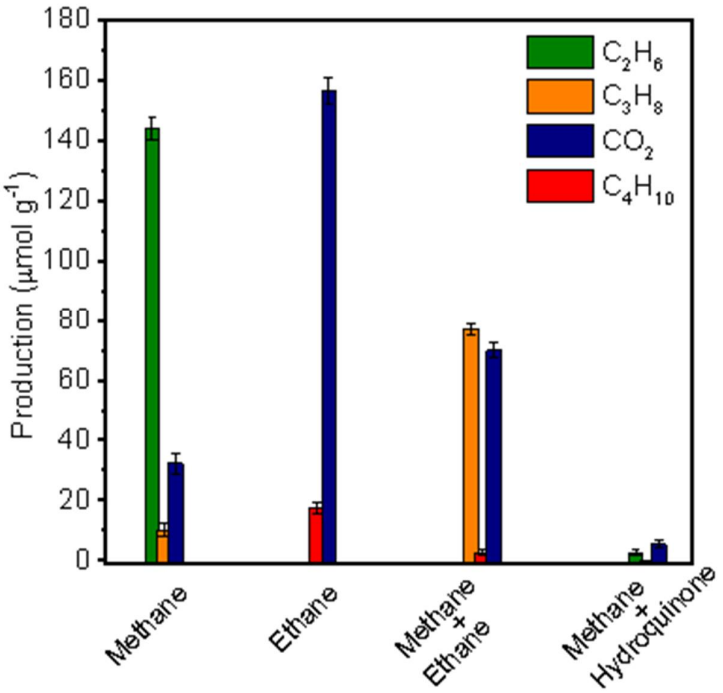

Figure 5. Photochemical coupling of methane and ethane on Ag-HPW/TiO_2. Reaction conditions: catalyst, 0.1 g; gas phase pressure, CH_4 0.3 MPa; C_2H_6 0.3MPa; CH_4 0.285 MPa, C_2H_6 0.015 MPa; CH_4 0.3 MPa, respectively, irradiation time, 7 h. Hydroquinone: radical scavenger. The selectivity was calculated on a molar carbon basis. The experiments in each case were performed for three times. The error bar represents the relative standard deviation, which is within 5%.

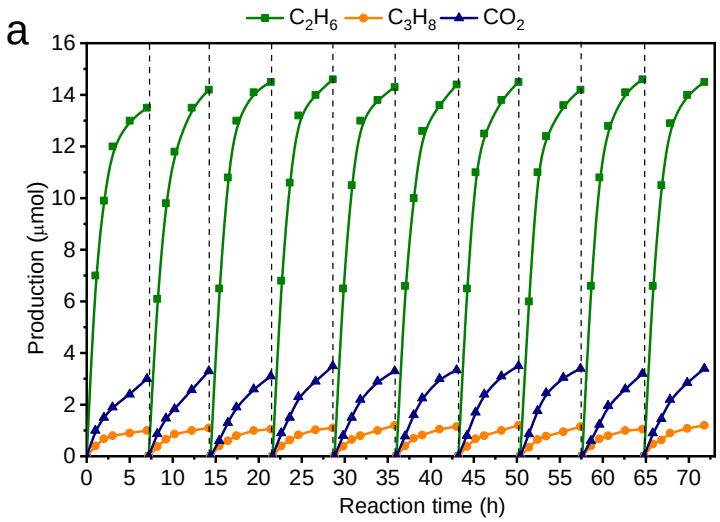

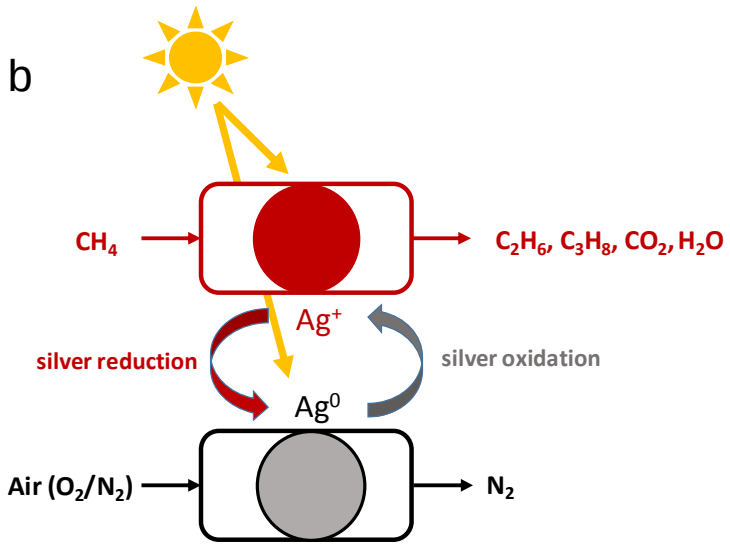

Figure 6. Reaction and regeneration of Ag-HPW/TiO_2 : (a) Reaction-regeneration cycles in methane photochemical coupling on Ag-HPW/TiO_2, The solid lines are guides to the eye. Dashed lines represent catalyst regeneration (b) Schematic description of photochemical looping process. Reaction conditions: catalyst, 0.1 g; gas phase pressure, CH_4 0.3 MPa.